



HAL
open science

Chiral Spiro-Tetrathiafulvalenes: Synthesis, Chiroptical Properties, Conformational Issues and Charge Transfer Complexes

Alexandra Bogdan, Ionut-Tudor Moraru, Nicolas Vanthuyne, Pascale Auban-Senzier, Ion Grosu, Narcis Avarvari, Flavia Pop

► **To cite this version:**

Alexandra Bogdan, Ionut-Tudor Moraru, Nicolas Vanthuyne, Pascale Auban-Senzier, Ion Grosu, et al.. Chiral Spiro-Tetrathiafulvalenes: Synthesis, Chiroptical Properties, Conformational Issues and Charge Transfer Complexes. *Chemistry - A European Journal*, 2024, 30 (29), 10.1002/chem.202400564 . hal-04786254

HAL Id: hal-04786254

<https://univ-angers.hal.science/hal-04786254v1>

Submitted on 15 Nov 2024

HAL is a multi-disciplinary open access archive for the deposit and dissemination of scientific research documents, whether they are published or not. The documents may come from teaching and research institutions in France or abroad, or from public or private research centers.

L'archive ouverte pluridisciplinaire **HAL**, est destinée au dépôt et à la diffusion de documents scientifiques de niveau recherche, publiés ou non, émanant des établissements d'enseignement et de recherche français ou étrangers, des laboratoires publics ou privés.



Distributed under a Creative Commons Attribution 4.0 International License

Chiral Spiro-Tetrathiafulvalenes: Synthesis, Chiroptical Properties, Conformational Issues and Charge Transfer Complexes

Alexandra Bogdan,^[a,b] Ionut-Tudor Moraru,^{*[c]} Nicolas Vanthuyne,^[d] Pascale Auban-Senzier,^[e] Ion Grosu,^[b] Narcis Avarvari,^{*[a]} and Flavia Pop^{*[a]}

[a] *Univ Angers, CNRS, MOLTECH-Anjou, SFR MATRIX, F-49000 Angers (France)*

E-mail: flavia.pop@univ-angers.fr; narcis.avarvari@univ-angers.fr

[b] *Babes-Bolyai University, Faculty of Chemistry and Chemical Engineering, Department of Chemistry and SOOMCC, Cluj-Napoca, 11 Arany Janos Str, 400028, Cluj-Napoca (Romania)*

[c] *Babes-Bolyai University, Faculty of Chemistry and Chemical Engineering, Department of Chemistry, 11 Arany Janos Str, 400028, Cluj-Napoca (Romania)*

E-mail: ionut.moraru@ubbcluj.ro

[d] *Aix Marseille Université, CNRS, Centrale Marseille, UAR 1739, FSCM, Chiropole, Marseille (France)*

[e] *Université Paris-Saclay, CNRS, UMR 8502, Laboratoire de Physique des Solides, 91405 Orsay (France)*

Abstract

Within this work we have investigated spiro-based tetrathiafulvalenes (TTFs) obtained as mixtures of stereoisomers from racemic spiro[5.5]undeca-1,8-dien-3-one. Compared to previously described spiro-TTFs, enantiomeric and diastereoisomeric forms have been here separated by chiral HPLC and fully characterized both experimentally and theoretically. The two types of spiro-based chiral derivatives contain either one (**2**) or three (**1**) chiral centres out of each one is spiro-type. Experimental CD, supported by TD-DFT calculations, shows differences in the optical activity between the **1** and **2** and their intermediates. The low optical activity of **2** and **3** (spiro alone chirality) was attributed to the presence of two conformers in the solution (*ax* and *eq*) of opposite Cotton effect whereas in the case of **1** and **5** (spiro and stereogenic centres) the spiro

chirality seems to be responsible of the Cotton effect in the high energy region whereas the *R* and *S* chirality in the low energy region. Racemic and enantiopure forms have been successfully used for the synthesis of charge transfer complexes with tetracyanoquinodimethane (TCNQ) based acceptors.

Introduction

Chiral electroactive materials^[1] are gaining continuous interest in the frame of chirality related physical phenomena such as the electrical magnetochiral anisotropy (eMChA) effect or the chirality induced spin selectivity (CISS) effect. eMChA effect expresses the dependence of the resistance of a chiral conductor on its handedness and on both the relative orientation of the electrical current and the applied magnetic field,^[2,3] whereas the CISS effect refers to the selective transmission of a preferential electron spin orientation through a chiral material.^[4,5,6] Similarities and differences between the two effects have been recently discussed.^[7] Note also the interest of chirality in superconductors,^[8,9] with recent evidence of eMChA^[10] and CISS.^[11] One of the most convenient molecular electroactive platform for chiral functionalization is tetrathiafulvalene (TTF),^[12] and especially ethylenedithio-tetrathiafulvalene (EDT-TTF)^[13,14] and bis(ethylenedithio)-tetrathiafulvalene (BEDT-TTF),^[15,16] on which stereogenic centers can be created by substitution of hydrogen atoms of the ethylene bridge to provide, for example, chiral alkylated derivatives. Such compounds have been used as precursors for various conducting radical cation salts or charge transfer (CT) complexes as enantiopure and/or racemic forms.^[17,18,19,20,21] Alternatively, chiral counterions can be used in combination with achiral TTF donors to provide enantiopure conductors.^[11,22,23,24] Nevertheless, eMChA has been observed so far only in one pair of TTF based crystalline enantiomeric conductors, namely (DM-EDT-TTF)₂ClO₄ (DM-EDT = dimethyl-ethylenedithio),^[25] while CISS was very recently detected with the DM-BEDT-TTF and TM-BEDT-TTF (TM = tetramethyl) precursors by electrochemical measurements.^[26] It is therefore of great importance to address different types of chirality in the TTF precursors in order to: *i*) allow access to a large library of chiral conductors which can show exotic chirality related phenomena; *ii*) correlate the type of chirality, chiroptical response and the magnitude of the eMChA/CISS effects. Noteworthy, with respect to the CISS effect, it has been shown that the chiroptical activity and the spin polarization properties are intimately linked.^[27,28] Beside the point chirality, axial chirality has been also introduced in TTF precursors such as TTF-

helicenes,^[29] TTF-allenes^[30] or TTF-binaphthyl^[31,32] derivatives which have shown interesting chiroptical properties. Another interesting platform through which axial chirality can be addressed is the spirane unit,^[33] yet the number of reported TTF-spiranes is still limited to date (Figure 1).

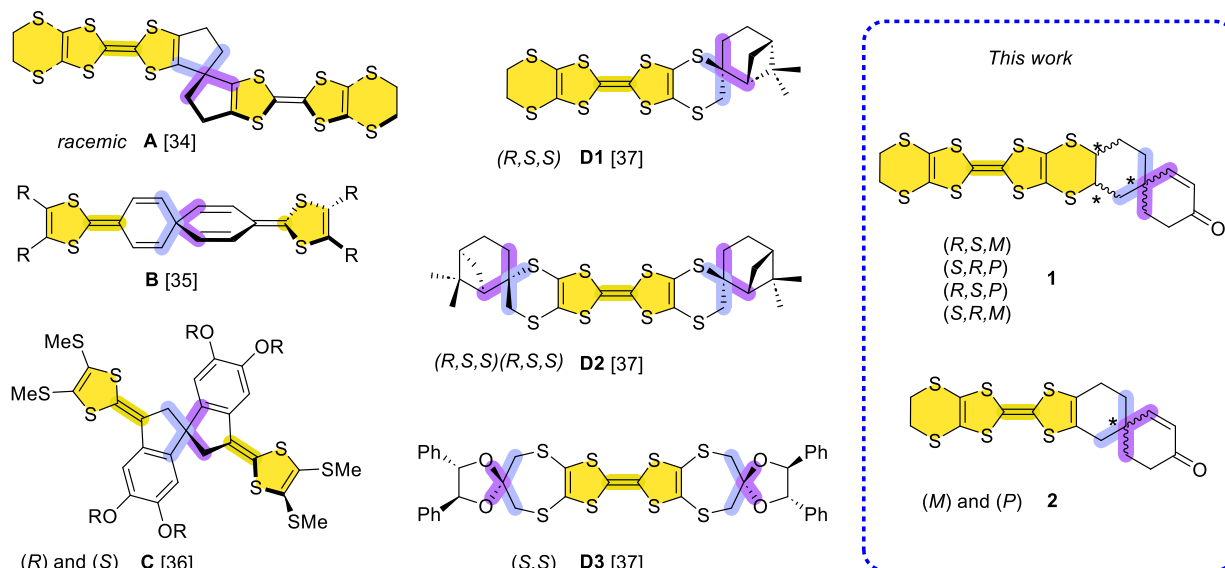


Figure 1. TTFs containing spiro-framework described in the literature; those described in this work are highlighted with the blue rectangle.

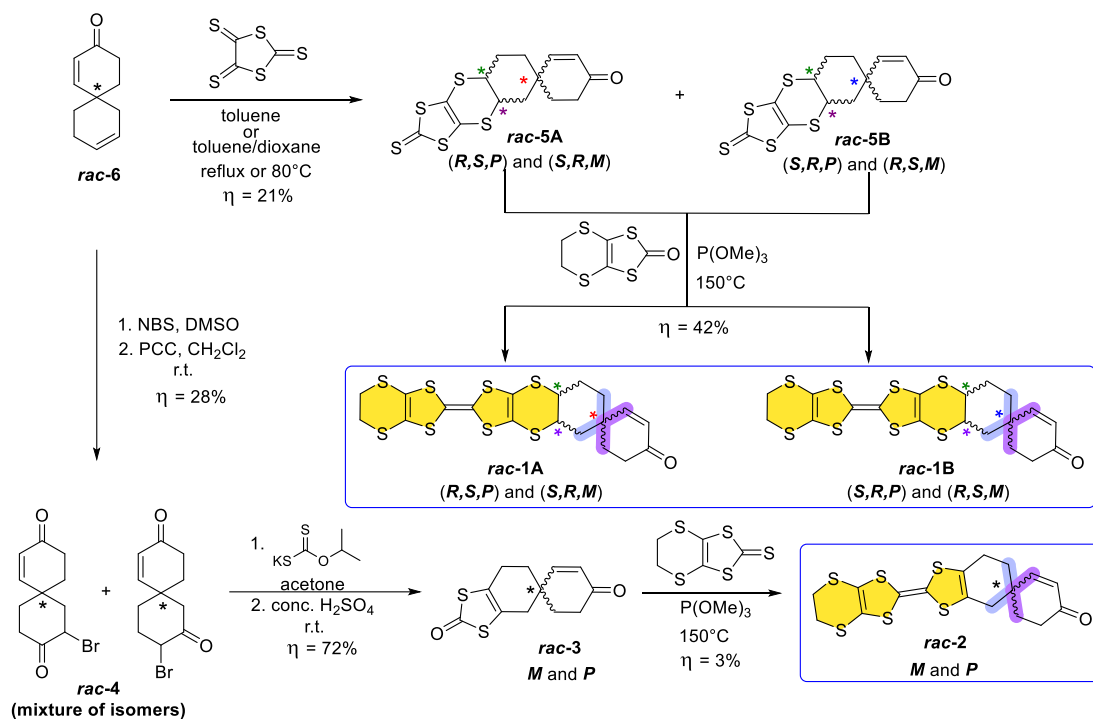
Accordingly, Tatemitsu *et al.* reported for the first time in 1986 spiro-TTFs of type **A** (Figure 1), though without any mention to chirality.^[34] These compounds were used in charge transfer complexes with DDQ (2,3-Dichloro-5,6-dicyano-*p*-benzoquinone) as acceptor. Much later, symmetric spiro-conjugated bis(dithiafulvenes) of type **B** (Figure 1) have been reported by Martín *et al.*^[35] However, due to the electrochemical instability of the oxidized species, they could not be further used as precursors for radical cation salts or CT complexes. Another example of spiro-extended-TTF **C** (Figure 1) was reported by Hasegawa *et al.*,^[36] on which, despite the stepwise oxidation of the two TTF units during the cyclic voltammetry measurements, only formation of dicationic species was observed by chemical oxidation, suggesting a certain instability of the monocation. Another drawback of the spiro-TTFs **B-C**, beside their electrochemical instability, is their complex multi-step synthetic strategy. A much simpler synthetic strategy was reported by Wallis *et al.* for the introduction of spiro units onto the TTF skeleton in compounds **D1-D3** (Figure 1).^[37] However, besides the synthesis and cyclic voltammetry measurements, no chirality related investigations, such as circular dichroism (CD), were reported on these spiro-TTFs.

The very few literature reports on spiro derivatives decorated with TTF reveal some drawbacks such as multi-step synthesis and electrochemical instability, but their chiroptical properties and potential for chiral materials is yet to be revealed. In this context, we report herein the straightforward synthesis, solid state structures and chiroptical properties, supported by in-depth TD-DFT calculations and interpretations, of the spiro-BEDT-TTF **1** and spiro-EDT-TTF **2** (Figure 1), together with those of their precursors. Our study has a particular focus on the conformational issues related to the presence of the six-membered rings in the spiro units and their influence on the chiroptical response. The role and the consequences of the number of stereogenic centers together with preliminary results on the preparation and structural characterization of CT complexes of donor **2** with tetracyanoquinodimethane (TCNQ) derivatives are presented as well.

Results and Discussion

Synthesis and characterization

The key molecule for the synthesis of spiro-TTFs, either with one or three chiral centres, is the previously reported spiro[5.5]undeca-1,8-dien-3-one (**6**)^[35] which has been used as racemic mixture (Scheme 1). The Diels-Alder pericyclic reaction of **6** with 1,3-dithiolane-2,4,5-trithione afforded a mixture of four stereoisomers (21% yield) which could be partially separated by conventional chromatography in two diastereoisomeric mixtures of enantiomers *rac*-**5A** and *rac*-**5B**. The synthesis of the *rac*-**3** has been done in four steps from **6** following procedures adapted from literature.^[34,38] The addition reaction with N-bromosuccinimide (NBS) followed by oxidation with pyridinium chlorochromate (PCC) afforded *rac*-**4** as mixtures of isomers in 63% yield. The substitution of the bromine with isopropyl xanthate followed by cyclization with concentrated sulfuric acid afforded spiro-dithiocarbonate **3** as racemic mixture in 75% yield. The phosphite-mediated heterocoupling between the racemics of **5A**, **5B** and **3** and the ethylenedithiol-1,3-dithiol-2-one and 2-thione, respectively, afforded the corresponding spiro-TTFs **1A**, **1B** and **2** as racemic mixtures (NMR details in Figures S1 – S20).



Scheme 1. Synthetic routes to spiro-TTFs **1** and **2**.

The $^1\text{H-NMR}$ spectra of both diastereoisomeric mixtures of enantiomers **rac-5A** and **rac-5B** show a set of two signals with a coupling constant of ~ 10.3 Hz, corresponding to the double bond near the carbonyl group. The signals of protons H_a , H_b and H_c are deshielded for the **rac-5A** derivative with respect to the **rac-5B** derivative by 0.4, 0.1 and 0.1 ppm, respectively and they have been assigned based on 2D HSQC and HMBC-NMR spectra (Figure 2 and ESI for details).

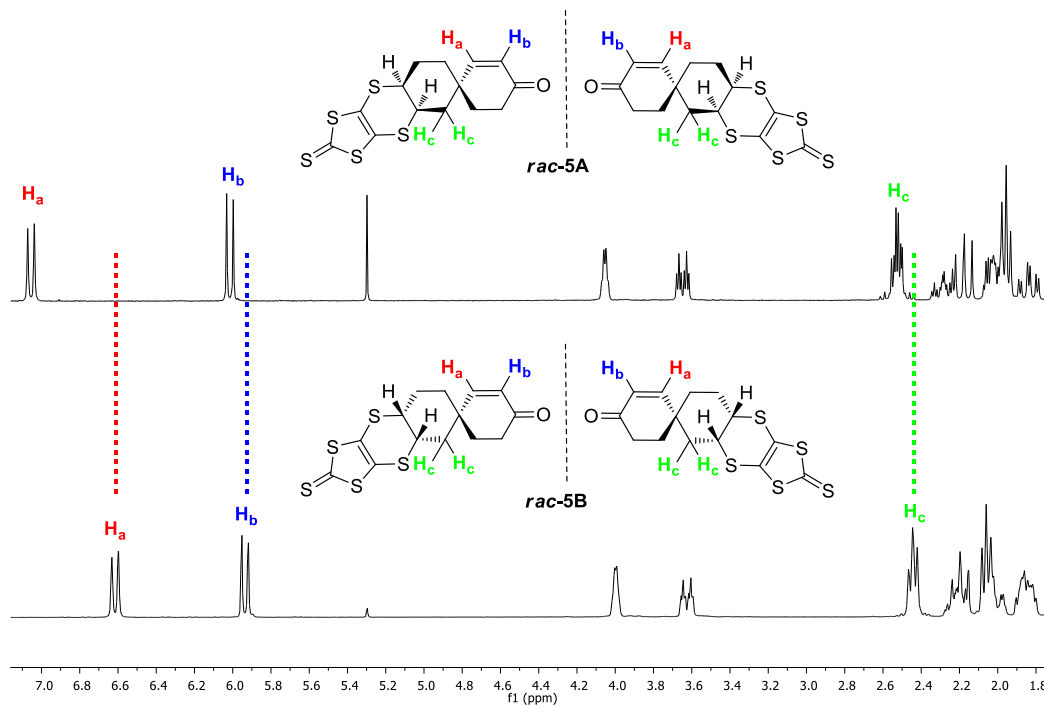


Figure 2. $^1\text{H-NMR}$ spectra of *rac-5A* and *rac-5B* (300 MHz, CDCl_3).

Enantiomer resolution and chiroptical characterization

Enantiomers of both *rac-5A*, *rac-5B* and *rac-3* have been successfully separated by chiral HPLC technique, on a Chiralpak IH column, using ethanol/dichloromethane (50/50) as mobile phase, with an ee > 99.5% for each enantiomer (see ESI for details). The pairs of enantiomers exhibit the same UV-Vis absorption pattern with maxima in the range of 400 - 410 nm for **5** and 280 nm for **3**. Although in the crystal they have intense yellow (for *rac-5A*) and orange (for *rac-5B*) colours, in solution only a 5 nm shift is observed (Figure 3). Measurements reveal a difference of about 200 degrees in the optical rotation values between the two sets of isomers, **5B** exhibiting a higher optical activity with respect to **5A**. The difference in the optical activity is even higher between **3** and **5** where the spiro alone chirality in **3** is showing a much lower optical activity than the three chiral centres in **5** (Table S1 and S2).

The mirror-image pattern of the CD spectra confirmed the enantiomeric relation between the isolated forms of **5** and **3** (Figures S21 and S22). While the same UV behaviour is noticed in the entire range of activity, substantial differences can be observed between the CD spectra of the two pairs of enantiomers of **5** between 190 – 340 nm. Even though all stereoisomers display the same

wave features between 350 – 500 nm, the first eluted enantiomer of **5A** (green line – Figure S21 up left panel) presents a positive – to – negative Cotton effect, while the first eluted enantiomer of the **5B** pair (green line – Figure S21 up right panel) presents a negative – to – positive Cotton effect. DFT calculations were performed in order to establish the absolute configuration of the separated stereoisomers and to properly assign the spectroscopic experimental data (*vide infra*).

The TTF-spiranes **1**, containing the two diastereoisomeric pairs *rac*-**1A** / *rac*-**1B**, and *rac*-**2** have been successfully separated by chiral HPLC using ethanol/dichloromethane (50/50) as mobile phase on Chiralpak IH and Chiralpak IC columns with an ee > 99.5%. The resolution of the complex mixture of **1** required a first elution on Chiralpak IH which allowed separation of the two enantiomers of **1A**, namely **1A1** and **1A2**, and of *rac*-**1B**, followed by the separation of the latter on Chiralpak IC to afford the two enantiomers **1B1** and **1B2** (see the HPLC details in the ESI). The UV-Vis absorption spectra of the four stereoisomers are identical, whereas the pattern of the CD is different between the diastereoisomeric isomers, as also noticed for their precursor **5** (Figure 3 and S21). However, the optical rotations of the spiro-TTFs show a difference of -200 degrees compared to the corresponding precursors **5**, whereas this difference in the optical activity is retrieved as well between the diastereoisomers **A** and **B** of both **1** and **5** (Tables S1 and S3). Moreover, the CD spectroscopy and optical rotation measurements reveal a very low optical activity of the enantiopure compounds **2A** and **2B** compared to **1A** and **1B**, similar to their precursors **3** and **5**, respectively (Figure S23 and Tables S2 and S4).

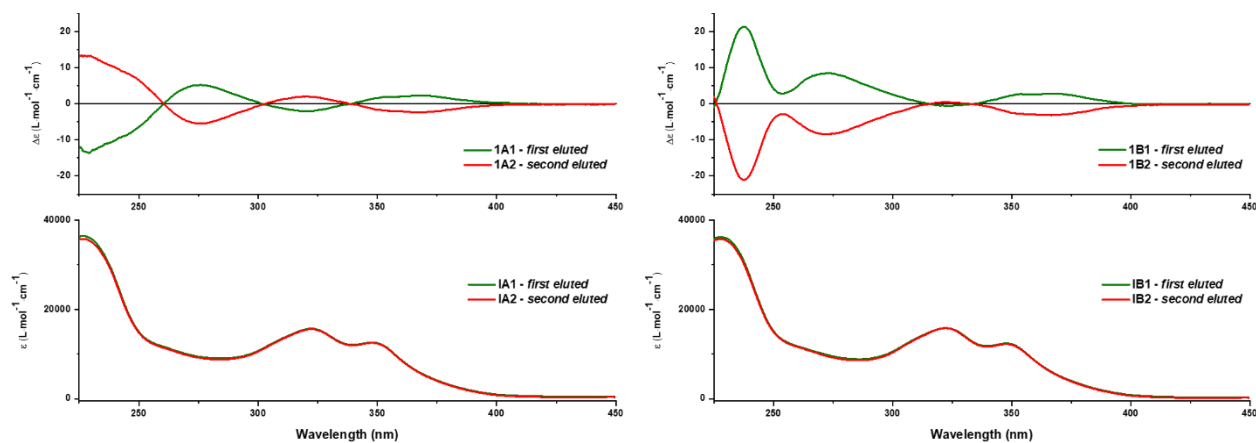


Figure 3. CD (top panels) and UV-Vis (bottom panels) spectra of enantiomers of **1A** (left) and **1B** (right) measured in dichloromethane, at room temperature (green line: first eluted enantiomer, red line: second eluted enantiomer).

Solid state characterization

Single crystals for X-ray diffraction measurements have been obtained by slow evaporation of mixtures of diethyl ether / dichloromethane for **rac-5A** and **rac-5B**, and dichloromethane / ethanol for **rac-3**. The crystals of the two diastereoisomeric mixtures **rac-5A** and **rac-5B** show yellow and orange colours, respectively, reflecting the different geometry and packing in the crystal. They crystallize with one independent molecule in the asymmetric unit, in the centrosymmetric space groups $P\bar{1}$ of the triclinic system for **rac-5A** and $C2/c$ of the monoclinic system for **rac-5B** and **rac-3** (Table S5, Figure S24). The two carbon atoms involved in the cycle of the spiro unit have the same *axial-equatorial* (*ax-eq*) conformations in all stereoisomers of **rac-5A** and **rac-5B**, imposed by the stereospecificity of the Diels-Alder reaction. The molecules of **rac-5A** close pack through short S...S contacts between EDT-DTT (4,5-ethylenedithio-1,3-dithiole-2-thione) units, where a sulfur atom from one molecule interacts laterally with two sulfur atoms from a second molecule (3.47-3.48 Å) and with a third alternating molecule (3.58 Å) (Figure S25, left). The packing of **rac-5B** shows columns of dyads between the spiro units (Figure S25, right). Due to the conformational arrangement of the EDT-DTT unit on the spiro core, the packing pattern is based on hydrogen bonding between the carbonyl group of one molecule and CH protons (2.34 Å) and CH₂ protons (2.39 Å) of the spiro units of two neighbouring molecules. In the structure of **rac-3** the molecules are disposed in columns of *head-to-tail* dithiolones with the bulky spiro units alternating sides (Figure S26). Intramolecular interactions consist of hydrogen bonding between the C=O of the dithiolone unit and one CH₂ of the spiro cycle (2.54 Å, magenta dotted lines) forming columns further interconnected by other O...H hydrogen bonding between the spiro units (blue dotted lines in Figure S26).

The first and second eluted enantiomers **5A1** and **5A2** have been crystallized by evaporation from a mixture of dichloromethane/ethanol = 1/1 solution and have been resolved in the non-centrosymmetric orthorhombic $P2_12_12$ space group (Figure S27 and Table S6). Their absolute configurations determined from the solid state structure analysis are *R,S,P* and *S,R,M*, respectively. The second eluted enantiomer of **rac-3** has been crystallized by evaporation from acetonitrile solution and has been resolved in the monoclinic $P2_1$ space group, with two independent molecules in the asymmetric unit. Based on the single crystal diffraction data, the absolute configuration of the second eluted fraction has been determined to be *M*. Thus, the two independent molecules in the asymmetric unit are conformers and correspond to *axial* and *equatorial* positions of the carbon

involved in the double bond, whereas in the case of *rac-3* only the *eq* conformer is present (Figure 4).

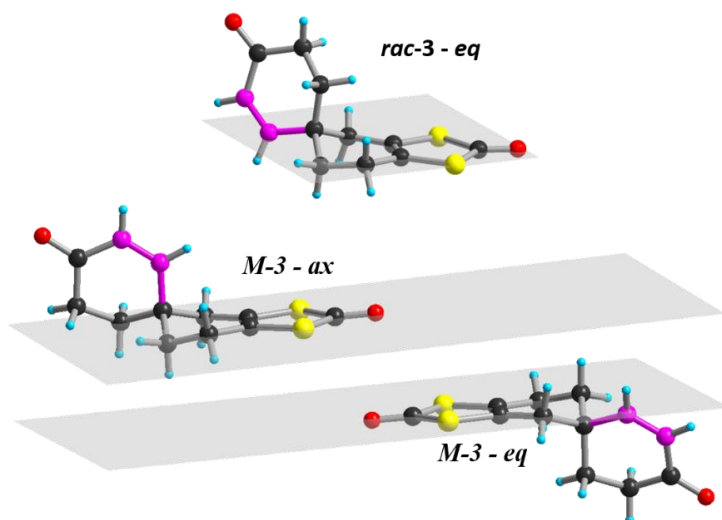


Figure 4. The two conformations, *axial* and *equatorial*, of the *M-3* enantiomer together with the structure of the racemic with *axial* conformation only.

Single crystals of the corresponding TTF derivatives *rac-1A*, *rac-1B* and *rac-2* have been obtained by slow evaporation of mixtures of dichloromethane/petroleum ether 1/3 and diethyl ether/dichloromethane 3/2. The *rac-1A* and *rac-1B* donors crystallize in the centrosymmetric triclinic $P\bar{1}$ and the non-centrosymmetric monoclinic P_C space groups with two (*rac-1A*) and four (*rac-1B*) independent molecules in the asymmetric unit, respectively, whereas *rac-2* crystallizes in the monoclinic centrosymmetric $P2_1/c$ space group, with one independent molecule in the asymmetric unit (Figure S28 and Table S7). The two independent molecules of *rac-1A* are alternating orthogonally and interact through $S\cdots S$ short contacts of 3.47, 3.57, 3.65 and 3.74 Å (Figure 5, blue circle). In the packing, each molecule of this repetitive motif is interacting laterally through $S\cdots S$ contacts with molecules with orthogonal arrangement (3.52 and 3.58 Å, green and red dotted lines) and with parallel arrangement (3.78 Å, pink dotted lines). *Rac-1B* crystallized with three molecules of *S,R,P* absolute configuration and one of *R,S,M* configuration (Figure 6, left). Two of the four molecules are disposed orthogonally to the other two in a *head-to-tail* manner, with an angle of $\sim 84^\circ$ between the TTF planes (Figure 6, right). Similar to *rac-1A*, the four molecules of the asymmetric unit interact through $S\cdots S$ short contacts 3.55 – 3.65 Å and 3.82 – 3.97 Å, either laterally or orthogonally (Figure S29). However, in the packing of *rac-1B* face-

to-face disposed molecules interact by CH₂-π contact ranging between 2.78-2.89 Å (Figure S29, pink dotted lines).

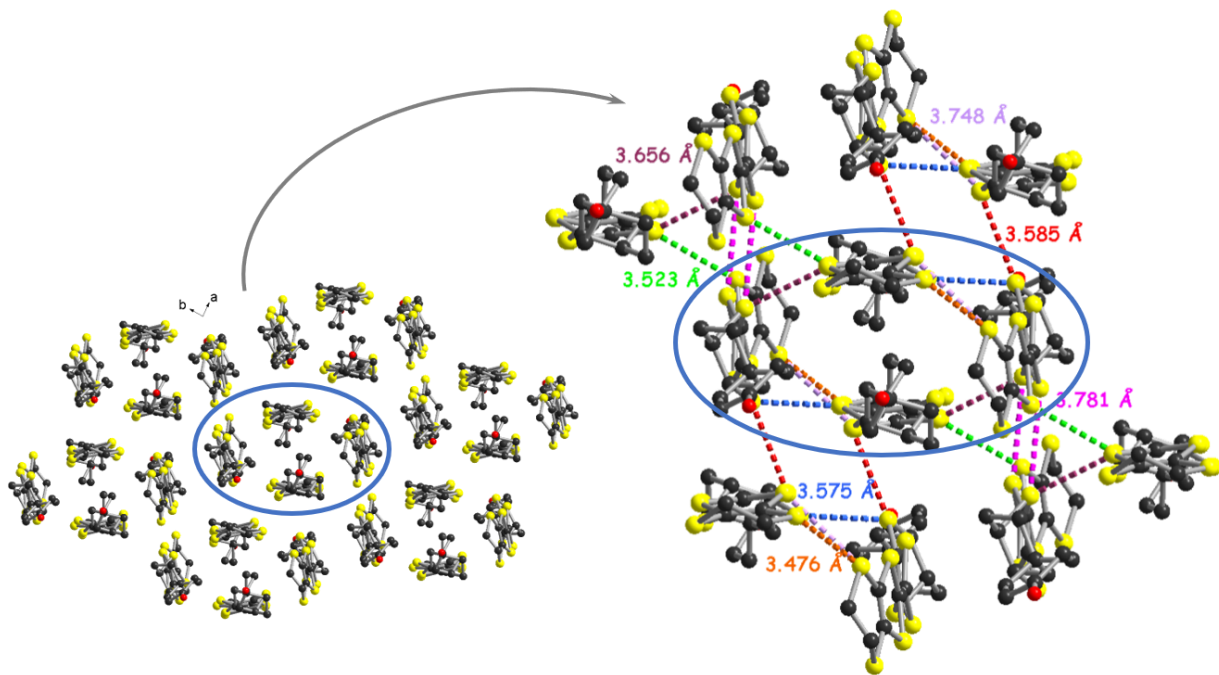


Figure 5. Crystal structure packing and highlight of S...S short interactions of *rac-1A*. Hydrogen atoms have been omitted for clarity.

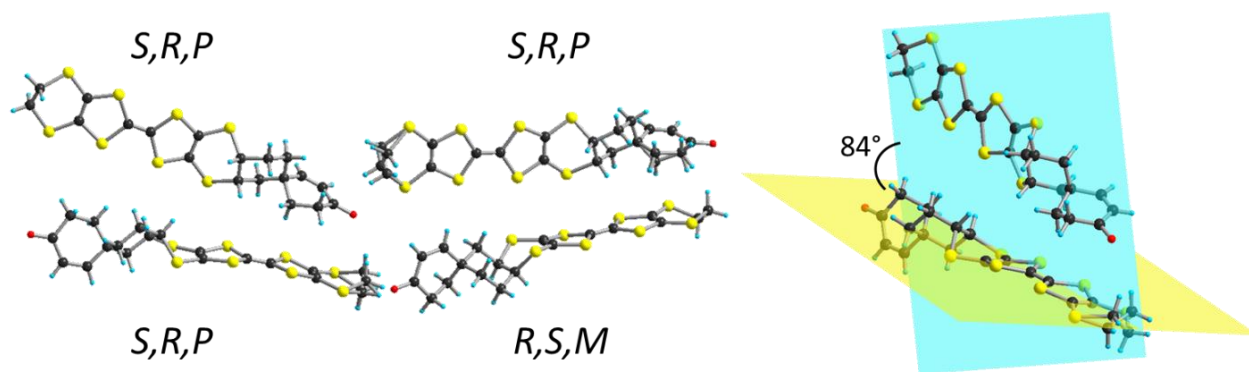


Figure 6. Enantio-enriched crystal structure of *rac-1B*.

In the packing of *rac-2* the spiro-TTF forms dimers through CH₂-π interactions between the spiro motif and the TTF unit (Figure 7, red dotted lines), with a herringbone disposition and *face-to-edge* interactions of O...S type between the dyads (Figure 7, blue dotted lines).

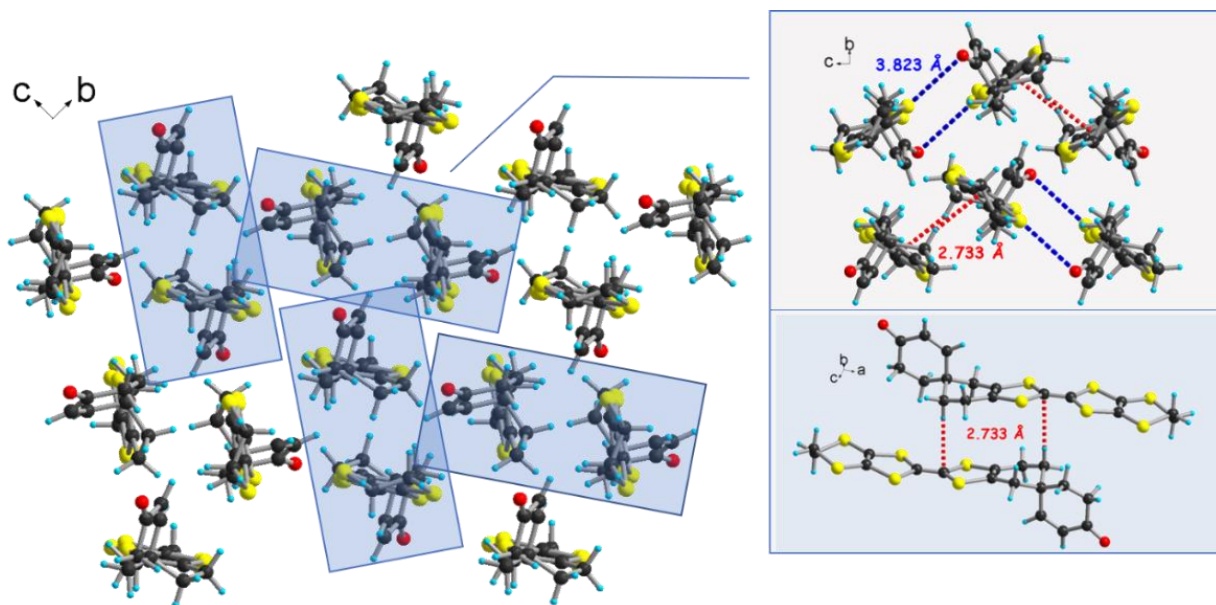


Figure 7. Dimer formation and disposition in the packing of *rac*-**2** together with a highlight of the short contacts.

Two of the stereoisomers of spiro-TTF **1** have afforded single crystals for X-ray diffraction by slow evaporation of a diethylether/chloroform 3/1 mixture of solvents. The enantiopure forms **1A2** and **1B1** crystallized in the non-centrosymmetric space group monoclinic $P2_1$, with the asymmetric unit composed of three independent molecules for the former and two molecules of spiro-TTF, two of water and one of chloroform for the latter. According to the solid state structure *S,R,M* and *R,S,M* absolute configuration, has been found for forms **1A2** and **1B1**, respectively (Figure S30 and Table S8). Both stereoisomers show *head-to-head* orientation in the *ac* plane (Figure 8). The *head-to-head* sheets of molecules are alternating along the *b* axis with an opposite orientation (Figure 9, left side) and short $S\cdots S$ interactions of 3.46 – 3.94 Å between molecules with *head-to-tail* arrangement (Figure 9, right side).

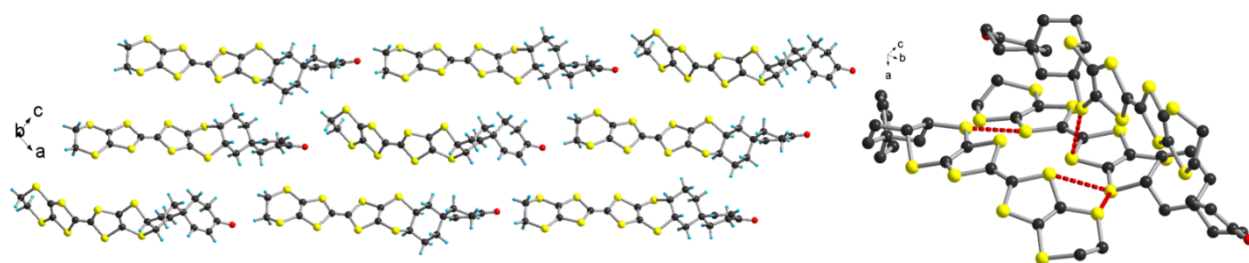


Figure 8. Packing diagram of **1A2** in the *ac* plane (left side) with a highlight of short $S\cdots S$ contacts (right side).

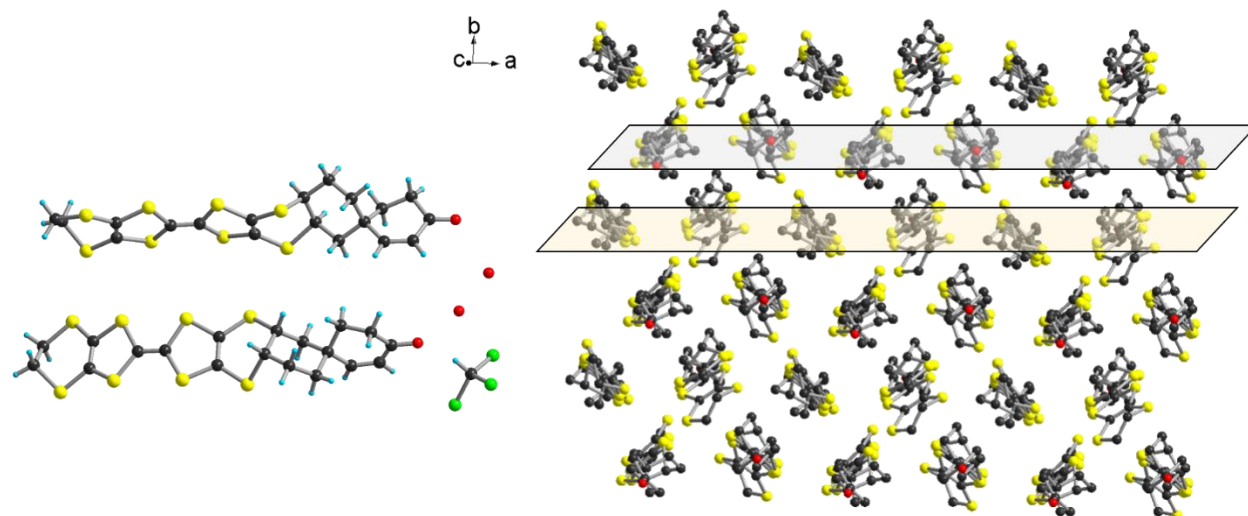


Figure 9. Asymmetric unit (left side) and packing diagram of **1B2** in the *ab* plane (right side).

DFT and TD-DFT investigations

Theoretical calculations were performed (*i*) to ensure the proper assignment of the absolute configuration for the investigated enantiomers and (*ii*) to gain further insights into their electronic and structural features. Given that in solution each enantiomer is expected to possess several conformations, due to fluxionality, a better understanding of their chiroptical properties requires a detailed conformational analysis beforehand.

Regarding diastereomers **5A** and **5B**, DFT calculations indicate that at room temperature four different conformers are relevant in each case. Their equilibrium geometries are illustrated in Figure 10, being highlighted that for all these conformers the cyclohexane ring adopts a chair conformation. Other possible conformers involving half-boat or boat conformations are at least 5 kcal mol⁻¹ higher in energy, leading to a low probability of finding them in solution at room temperature. Consequently, a detailed exploration of such unstable conformations is beyond the purposes of the current theoretical study. The investigated conformers of **5A** and **5B** share common features and thus, the following discussions regarding their structural characterization can be carried out simultaneously for both diastereomers. Conformer **5A_I** reveals as a distinctive feature the orientation of the C=C double bond of the spiro moiety in the *axial* position of the cyclohexane ring, while for **5B_I** the C=C double bond is placed equatorially (Figure 10). The possible formation of conformer **II** involves chair-chair interconversion of the cyclohexane unit of **I**, conformational change that requires *inter alia* the displacement of the C=C bond from *axial* to *equatorial* position in case of **5A**, and from *equatorial* to *axial* for **5B**. Conformer **III** results

from **II** via the flipping the dithio-dithiolate (DTDT) unit, the main difference between the two conformations being the relative orientation of the dithiolate moiety with respect to the C=C bond of the spiro fragment: *syn* for **5A_II**, *anti* for **5A_III**, and *vice versa* for the two **5B** conformers (see Figure 10). Conformation **IV** results from **III**, *via* the chair-chair interconversion of the cyclohexane ring, or from **I**, through the flipping of the DTDT unit. The main difference between **5A_IV** and **5B_IV** is the orientation of the C=C double, *axially* in the first one whereas in the second it occupies the *equatorial* position. According to the computed DFT energies, the most stable conformation of both **5A** and **5B** diastereomers is **IV**, although for **5A** the equilibrium geometry that best resembles the solid-state structure is that of conformer **I**. Nevertheless, the energy gap between **5A_I** and **5A_IV** is merely 0.2 kcal mol⁻¹, meaning that both conformers are expected to be found in solution in close ratios, in line with their calculated Boltzmann populations (Table S9). Regarding diastereomer **5B**, the equilibrium geometry of **IV** reproduces to a great extent the measured X-ray structure, while the computed energy of conformer **5B_I** is 0.4 kcal mol⁻¹ higher than that of **5B_IV**. Yet, both **5B_I** and **5B_IV** are expected to be present in solution at room temperature (Table S9). The calculated geometries of conformers **II** and **III**, of both **5A** and **5B** diastereomers, are noticeably higher in energy than those of **I** and **IV** (Figure 10). This results into significantly lower Boltzmann populations for the former and thus, a much lower probability of finding them in solution.

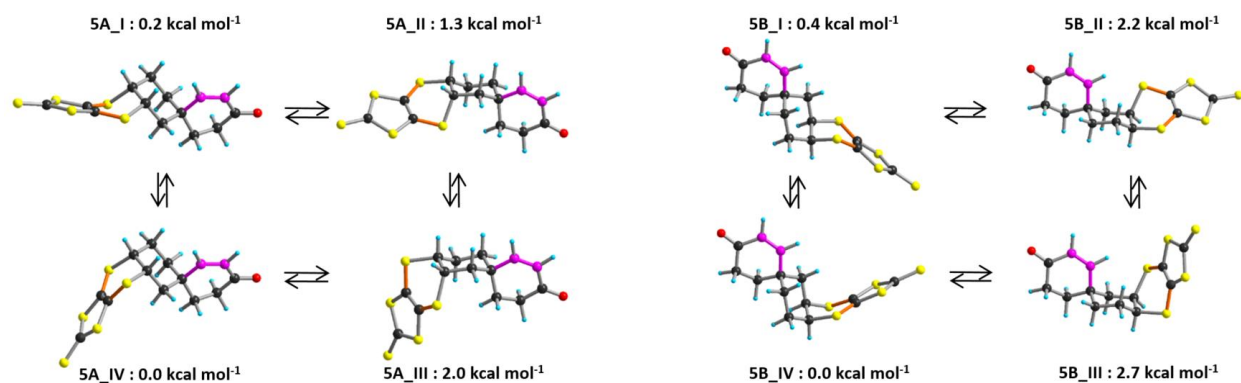


Figure 10. DFT optimized structures of the most relevant conformers of (*S,R,M*)-**5** (left) and (*R,S,M*)-**5** (right) enantiomers, together with their relative energies.

The absolute configurations of the investigated enantiomers were established after a systematic comparison between the crystallographic data, experimental CD spectra and calculated ones. The calculated absorption and CD spectra of diastereomers *S,R,M* and *R,S,M* were obtained as a

superposition of the Boltzmann-averaged spectra of each investigated conformer (Figure 11). According to the X-ray structure, the first eluted enantiomer (i.e., **5A1**) corresponds to the *R,S,P* enantiomer, while the second eluted one (i.e., **5A2**) corresponds to the *S,R,M* enantiomer, in agreement with the predicted CD spectra illustrated in Figure 11 for the *S,R,M* enantiomer. The assignment of the absolute configuration of enantiomers **5B1** and **5B2** was based solely on theoretical calculations. Hence, **5B1** (the first eluted) corresponds to the *S,R,P* enantiomer while **5B2** (the second eluted) to the *R,S,M* enantiomer. For both diastereomers, the second eluted enantiomer (**5A2** and **5B2**) displays *M* configuration of the spiro whereas the configuration of the asymmetric carbon is *S,R* and *R,S*, respectively (red dotted lines). From the experimental and calculated CD data it can be noticed that at low energies the Cotton effect is negative – to – positive for **5A2** and positive – to – negative for **5B2**. When comparing their CD spectra and the deduced absolute configurations we notice that the Cotton effect in the low energy area is mainly due to the *R,S* stereogenic centres, while the spiro unit is most probably responsible of the Cotton effect in the high energy range (Figure 11).

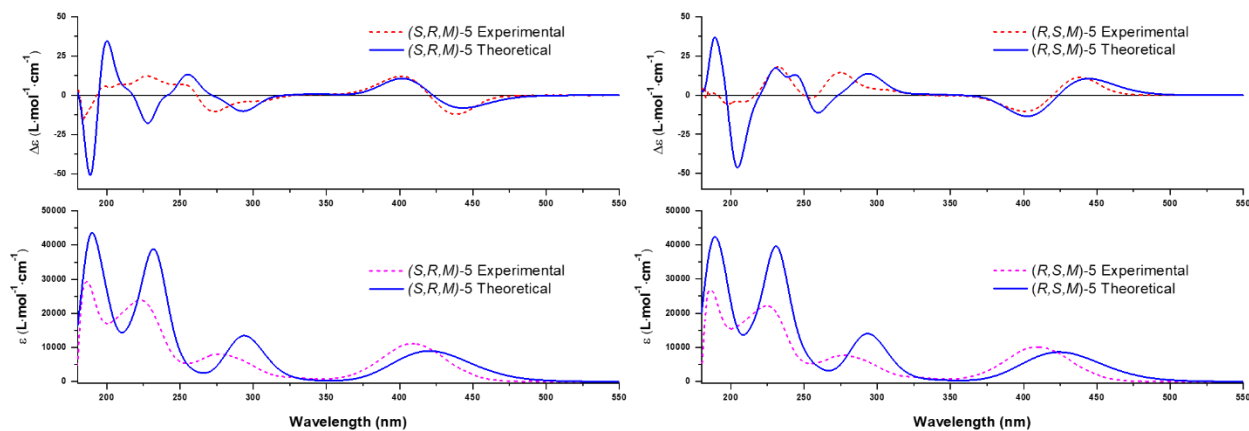


Figure 11. Experimental (dashed lines) and theoretical (solid lines) CD and UV-Vis absorption spectra of **5A2** (*left*) and **5B2** (*right*), together with the absolute configuration of investigated enantiomers.

The theoretical spectra of individual conformations (**I** to **IV**) are also illustrated (Figure S31). It is thus highlighted, for both diastereomers, that in the range of low-to-medium energies conformers **I** and **IV** afford CD signals of opposite sign compared to conformers **II** and **III**. However, given the low Boltzmann population of **II** and **III** (Table S9), these conformations contribute only in small ratios to the weighted-average spectrum. Consequently, the following discussion regarding the most relevant excitations for stereoisomers **5A2** and **5B2** will focus exclusively on conformers

I and **IV**. It is also shown by TD-DFT calculations that transitions occurring within the same conformation of different diastereomers have many common features (e.g., similar wavelengths, oscillator and rotatory strengths, orbital description and so forth) the main difference between them being the opposite sign of the CD signals.

For conformers **I** and **IV** (of both **5A2** and **5B2** diastereomers) the first two excitations afford intense signals in the absorption and CD spectra (Figures S32, S33 and Tables S10, S11). These transitions explain the experimental CD waves of opposite sign at *ca.* 435 and 400 nm, as well as the absorption band measured at *ca.* 410 nm. The absorption maximum is slightly redshifted for conformation **IV** compared to **I** (Figure S31). This is because within conformation **IV**, excitation $S_0 \rightarrow S_1$ allows more intense absorption signals than $S_0 \rightarrow S_2$, and vice-versa for conformer **I** (see Figure S33 and Table S10). To better understand these excitations, a detailed molecular orbital (MO) picture is required. Thus, in the case of conformer **5A_I**, excitation $S_0 \rightarrow S_1$ is roughly a HOMO-1 \rightarrow LUMO transition (*ca.* 70%), being described as a σ -to- π^* excitation from one of the lone pair electrons (LPs) at the sulfur atom (of the thione group) into a π^* orbital on the DTDT unit (relevant MOs are illustrated in Figure 12). The low oscillator strength of $S_0 \rightarrow S_1$ is explained in terms of a poor orbital overlap. Transition $S_0 \rightarrow S_2$ is mostly a HOMO \rightarrow LUMO excitation (*ca.* 70%), which reveals a considerably higher π - π character than the previous one. This excitation allows better orbital overlaps and thus an increased intensity in the absorption spectrum. For conformer **5A_IV**, the MO description of the first two excitations is somehow reversed, with $S_0 \rightarrow S_1$ being the HOMO \rightarrow LUMO transition (π - π , *ca.* 90%) and $S_0 \rightarrow S_2$ the HOMO-1 \rightarrow LUMO one (σ - π^* , *ca.* 90%). An even more convenient way to describe these excitations is based on natural transition orbitals (NTOs), since NTOs typically involve a single pair of orbitals per excitation and thus allowing a more insightful picture of electronic transitions (Figure 13). Regarding conformers **5B_I** and **5B_IV**, the $S_0 \rightarrow S_1$ and $S_0 \rightarrow S_2$ excitations behave similarly to those discussed above (for additional details, see Table S11 and Figures S33-S35).

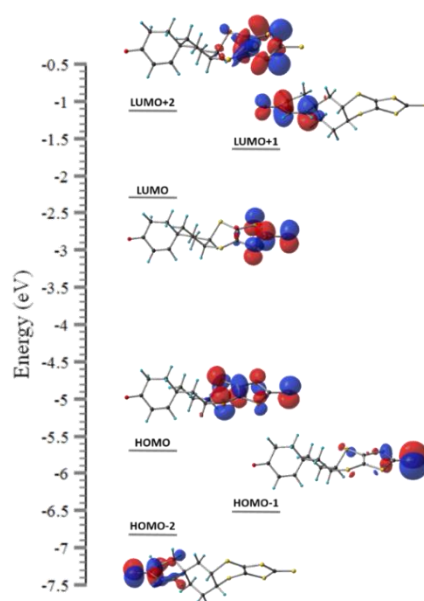


Figure 12. Selection of the most relevant MOs computed for conformer **5A_I**. **HOMO-2**: σ orbital on the spiro fragment containing a LP at the oxygen atom and the neighbouring $\sigma(\text{C-C})$ bonds. **HOMO-1**: σ orbital containing the LP of the sulfur atom (of the thionyl group) with minor contributions from vicinal $\sigma(\text{C-C})$ bonds of the DTDT ring. **HOMO**: π orbital on the DTDT unit and the thionyl group. **LUMO**: π^* orbital on the DTDT ring and the neighbouring thionyl group. **LUMO+1**: π^* orbital on the $\text{C}=\text{C}-\text{C}=\text{O}$ moiety of the spiro fragment. **LUMO+2**: σ^* orbital on the DTDT ring. Isosurface value = 0.04 a.u.; the frontier MOs computed for conformer **5A_IV** are similar to those illustrated above, while the MOs determined for conformers **5B_I** and **5B_IV** also reveal similar features (see Figure S34).

Other relevant transitions are $S_0 \rightarrow S_7$, for conformers **5A_I** and **5B_I**, and $S_0 \rightarrow S_8$, for conformers **5A_IV** and **5B_IV**, while excitation $S_0 \rightarrow S_9$ is relevant only for conformer **5B_IV** (see Figures S32 and S33). These excitations explain the absorption band and the CD wave measured at *ca.* 280 nm, although their calculated wavelengths are slightly redshifted with respect to the experimental maxima (comparisons between theory and experiment are illustrated in Figures 11 and S31). The molecular orbital description of these transitions is rather complex, since each of them involves at least three sets of MOs (Tables S10, S11). Based on the NTO analysis it is shown that both $S_0 \rightarrow S_7$ (of conformer **5A_I**) and $S_0 \rightarrow S_8$ (of conformer **5A_IV**) excitations represent $\pi-\pi$ transitions occurring within the DTDT moiety (Figure 13c and 13f), their increased orbital overlaps affording intense signals in the absorption spectrum. The same excitations occurring in conformers **5B_I** and **5B_IV** have similar description, while for the latter the experimental CD signal around 280 nm is explained by several transitions of moderate intensity (i.e., $S_0 \rightarrow S_6$, $S_0 \rightarrow S_7$, $S_0 \rightarrow S_8$ and

$S_0 \rightarrow S_9$), and not by a single excitation as in the other conformations (Figures S33 and S35, Table S11).

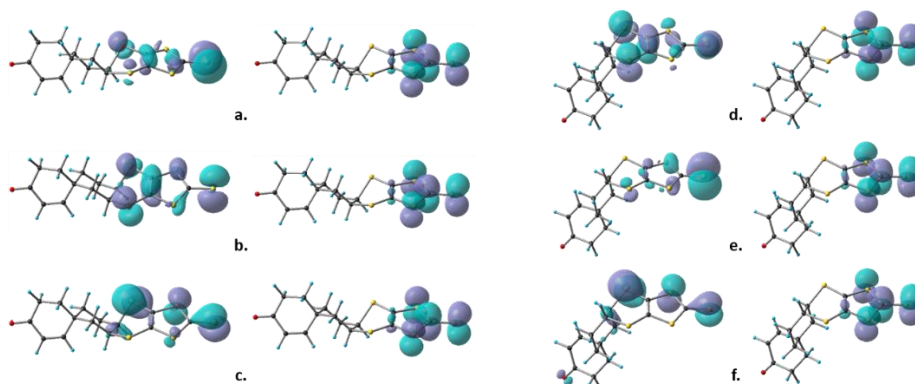


Figure 13. Natural transition orbitals describing several excitations occurring within conformations **I** and **IV** of **5A1**. (a) $S_0 \rightarrow S_1$, (b) $S_0 \rightarrow S_2$ and (c) $S_0 \rightarrow S_7$ transitions of conformer **5A_I**, and (d) $S_0 \rightarrow S_1$, (e) $S_0 \rightarrow S_2$ and (f) $S_0 \rightarrow S_8$ excitations of conformer **5A_IV**. Isosurface value = 0.04 a.u.; for conformers **5B_I** and **5B_IV**, the NTOs involved in the most relevant excitations are similar (see Figure S35).

DFT calculations of the spiro-TTFs (**1A** and **1B**) have been carried out only on the molecular geometries imported from the solid-state, without performing a detailed conformational study due to their more complex structures. Considering the results obtained with their precursors, **5A** and **5B**, similar behaviour is expected for stereoisomers **1A** and **1B**. In this case one enantiomer of each mixture, **1A2** and **1B1**, has been characterised by single crystal X-ray diffraction. The absolute configuration of the first eluted enantiomer **1A1** is identical to the first eluted one of the precursor **5A1**, whereas the first eluted enantiomer **1B1** of the other mixture has opposite configuration (R,S,M) to its precursor **5B1** (S,R,P) (Figure 14). From the experimental and calculated CDs we can observe that the first eluted enantiomer of each mixture, **1A1** and **1B1** (green and red lines, respectively), present a first positive Cotton effect in accordance with the R,S absolute configuration of the stereogenic atoms.

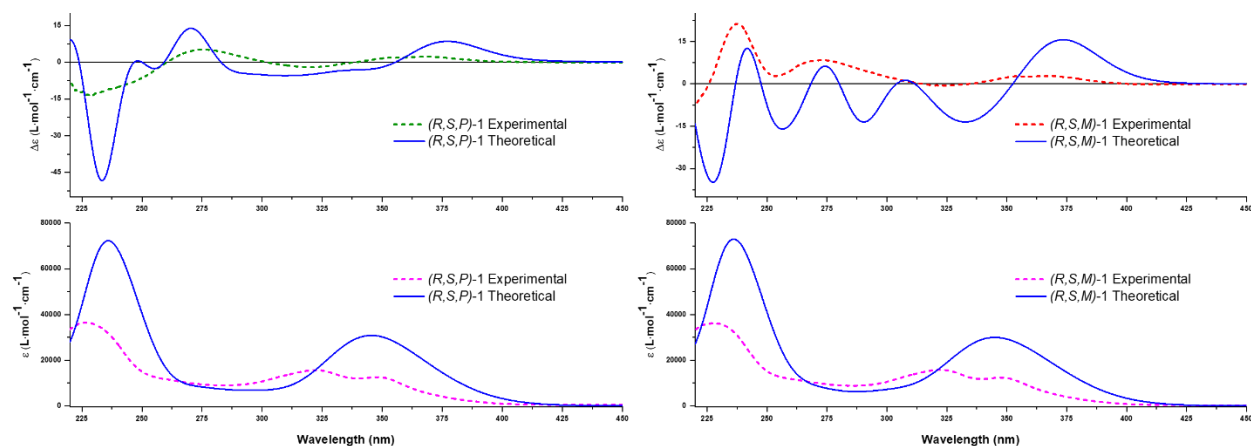


Figure 14. Theoretical (solid lines) and experimental (dashed lines) CD and UV-Vis absorption spectra of **1A1** (*left*) and **1B1** (*right*), together with the absolute configuration of investigated enantiomers.

The theoretical UV-Vis and CD spectra of **1A** and **1B** largely reproduce the experimental measured ones (Figure 14). For both diastereomers, excitations $S_0 \rightarrow S_1$ (i.e., HOMO \rightarrow LUMO+1), a π -to- σ^* transition on the TTF unit, and $S_0 \rightarrow S_2$ (i.e., HOMO \rightarrow LUMO), a π - π^* transition from the TTF unit into the C=C-C=O moiety on the spiro fragment, are silent in both absorption and CD spectra (MOs are illustrated in Figure 15). However, the following three singlet states provide more intense signals. Excitation $S_0 \rightarrow S_3$ affords the positive experimental CD wave between 350 and 400 nm, while $S_0 \rightarrow S_5$, together with transitions $S_0 \rightarrow S_4$ and $S_0 \rightarrow S_3$, explain the adsorption bands measured in the range of low energies (see Figure S36). These transitions are difficult to characterize in terms of canonical MOs, since each of them involves at least three different pairs of such orbitals (Tables S12 and S13).

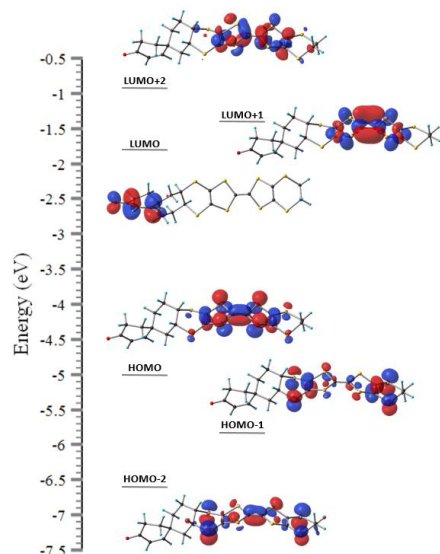


Figure 15. Selected MOs for enantiomer **1A1**. **HOMO-2**: π orbital extended on the BEDT-TTF moiety. **HOMO-1**: π orbital mostly on the lateral sides of the BEDT-TTF moiety. **HOMO**: π orbital on the TTF unit. **LUMO**: π^* orbital on the C=C-C=O moiety of the spiro fragment. **LUMO+1**: σ^* orbital on the TTF unit. **LUMO+2**: π^* orbital on the TTF unit. Isosurface value = 0.04 a.u.; the MOs computed for **1B** are similar (for comparisons see Figure S37).

NTO analyses reveal that both $S_0 \rightarrow S_3$ and $S_0 \rightarrow S_5$ are basically π - π transitions on the BEDT-TTF moiety (Figure 16a, c). The increased orbital overlap for $S_0 \rightarrow S_5$ is in line with the high oscillator strength computed for this transition. Excitation $S_0 \rightarrow S_4$ is more complex since it is described by two pairs of NTOs. It involves both the σ - π^* and π - π^* transitions occurring within the TTF unit (Figure 16b1, b2). Excitations $S_0 \rightarrow S_7$ and $S_0 \rightarrow S_9$ are also relevant for diastereomer **1A**, while $S_0 \rightarrow S_8$ for **1B**. These transitions, along with $S_0 \rightarrow S_5$, afford the moderate-to-low intensity experimental CD wave between *ca.* 300 and 350 nm. According to NTO calculations, both $S_0 \rightarrow S_7$, $S_0 \rightarrow S_9$ (of diastereomer **1A**) and $S_0 \rightarrow S_8$ (of diastereomer **1B**) occur on the BEDT-TTF unit, involving excitations from π orbitals to mixed- σ/π ones (Figure 16d, e). Other relevant excitations are $S_0 \rightarrow S_{20}$ (for **1A**) and $S_0 \rightarrow S_{19}$ (for **1B**), because they motivate the positive CD wave centred at *ca.* 275 nm (Figure S36 and Tables S12, S13). The NTO analysis reveal that these excitations occur on the lateral sides of the BEDT-TTF moiety (Figure 16f).

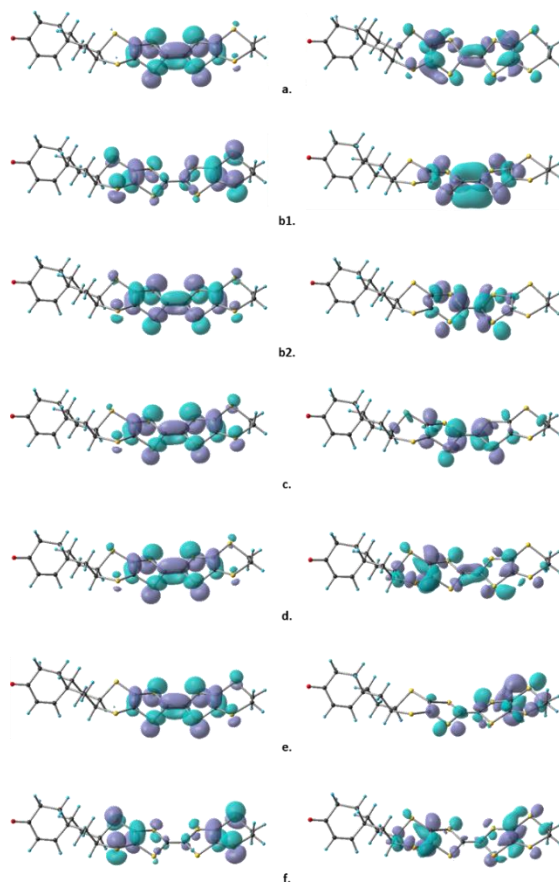


Figure 16. Natural transition orbitals involved in the most relevant mono-electronic excitations of enantiomer **1A1**. (a) $S_0 \rightarrow S_3$; (b1, b2) $S_0 \rightarrow S_4$; (c) $S_0 \rightarrow S_5$; (d) $S_0 \rightarrow S_7$; (e) $S_0 \rightarrow S_9$; and (f) $S_0 \rightarrow S_{20}$. Isosurface value = 0.04 a.u.; NTOs computed for **1B** are similar (for further details, see Figure S38).

Experimental results show lower dissymmetry factor (optical activity) of both spiro 1,3-dithiolone **3** and TTF **2** than the derivatives with both stereogenic carbons and spiro chirality **5** and **1** (Tables S1-S4). The existence of different conformers of a given stereoisomer could be the reason of the low intensity of the CD signals, as recently shown for chiral bis(dithiolene)Ni complexes.^[39] Crystallographic data, together with DFT calculations reveal that two conformers are relevant for **3**, namely **3-ax** and **3-eq**. The main difference between the two conformations is related to the spatial orientation of the C=C double bond (of the spiro unit) with respect to the central six-membered ring (Figure 17). The energy gap between **3-ax** and **3-eq** is merely 0.2 kcal mol⁻¹, meaning that at room temperature both conformers are present in solution in close ratios according to their calculated Boltzmann population (Table S14). Given that the two conformers exhibit CD

bands of opposite sign, this leads to the cancellation of CD signals (Figure 18) thus resulting into a low CD intensity of the experimental spectrum.

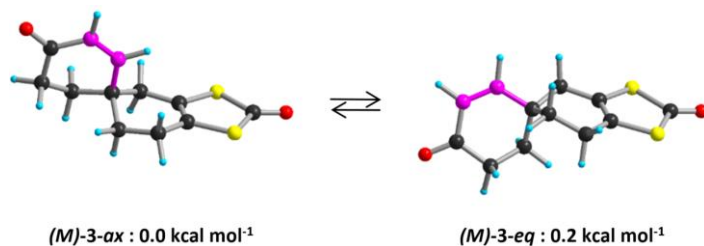


Figure 17. Equilibrium geometries of the two conformers of *M-3* and their relative energies.

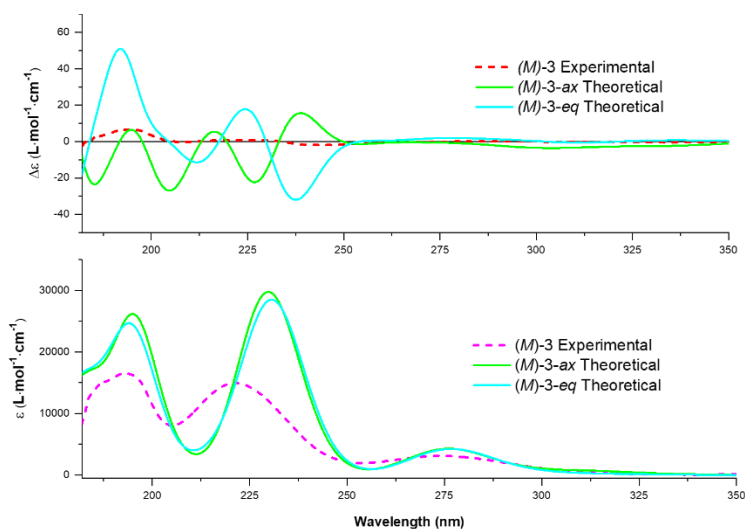


Figure 18. TD-DFT calculated CD (*above*) and UV-Vis absorption (*bottom*) spectra of *(M)-3-ax* and *(M)-3-eq* conformers of *(M)-3*. Experimental spectra of *(M)-3* are illustrated for comparisons.

The weighted-average UV-Vis and CD theoretical spectra of *(M)-3* largely reproduce the experimental ones (Figure S39). For *(M)-3-ax* and *(M)-3-eq* conformations, the most important excitations are summarized in Table S15. It is shown for both conformers that these transitions occur at a similar wavelength, exhibit comparable oscillator and rotatory strengths, and involve the same sets of canonical MOs, the main difference between them being the opposite sign of the CD signals. The first three excitations exhibit low intensities in the absorption spectrum, particularly $S_0 \rightarrow S_1$ and $S_0 \rightarrow S_3$ (Figure S40 and Table S15). This is due to the weak overlap between the orbitals involved in these excitations (relevant MOs are illustrated in Figure 19). Briefly, excitation $S_0 \rightarrow S_1$ (i.e., HOMO-1 \rightarrow LUMO) is a σ -to- π transition occurring on the spiro moiety, $S_0 \rightarrow S_2$ a π - π transition involving the frontier HOMO and LUMO orbitals, while $S_0 \rightarrow S_3$ a π - σ excitation occurring on the dithiolate unit that involves HOMO and LUMO+2 orbitals.

Although $S_0 \rightarrow S_2$ affords an increased absorption signal than the first and third excitations, the relatively low oscillator strength still computed for this state is motivated by the poor overlap between π MOs located in different regions of the space (see Figure 19). Regarding the CD spectrum, these excitations allow signals of moderate-to-low intensities. Excitation $S_0 \rightarrow S_4$ is a π - π transition occurring on the dithiolate ring, involving the HOMO and LUMO+1 orbitals. It affords a high intensity signal in the absorption spectrum because of the favourable MO overlap, but only weak CD activity. In fact, this excitation explains the experimental absorption maximum measured at *ca.* 275 nm (Figure 18 and S39). Other relevant excitations are $S_0 \rightarrow S_6$, $S_0 \rightarrow S_7$ and $S_0 \rightarrow S_9$, since $S_0 \rightarrow S_6$ and $S_0 \rightarrow S_9$ afford, for both (*M*)-**3-ax** and (*M*)-**3-eq** conformers, intense CD signals of opposite signs at 235 and 228 nm, while $S_0 \rightarrow S_7$ the absorption maximum measured at *ca.* 225 nm (Figure 18). From a MO perspective, transitions $S_0 \rightarrow S_6$ and $S_0 \rightarrow S_9$ are more complex, involving four different sets of MOs each (Table S15), while $S_0 \rightarrow S_7$ is broadly described by the HOMO-2 \rightarrow LUMO excitation, a π - π transition occurring within the C=C-C=O moiety of the spiro unit.

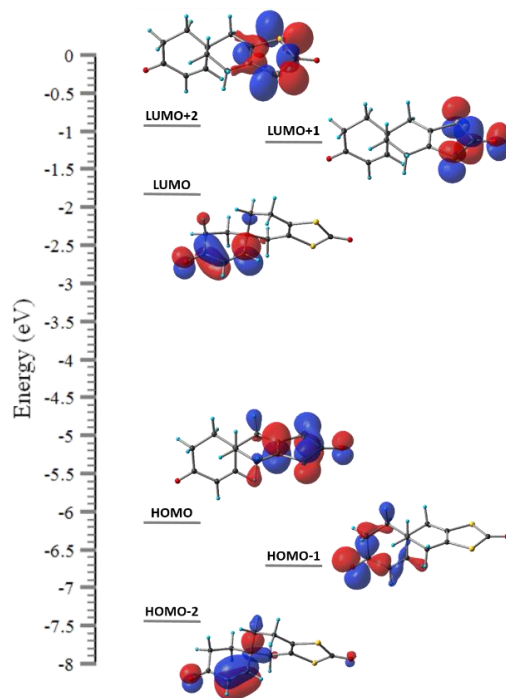


Figure 19. Selection of the most relevant MOs computed for the (*M*)-**3-ax** conformer. **HOMO-2**: π orbital on the spiro moiety located mainly on the C=C double bond and on the vicinal carbonyl group. **HOMO-1**: σ orbital on the spiro fragment and the lone pair electrons on the oxygen atom of the neighbouring carbonyl. **HOMO**: π orbital on the dithiolate ring and the vicinal carbonyl group. **LUMO**: π^* orbital on the C=C-C=O moiety of the spiro fragment. **LUMO+1**: π^* orbital on the dithiolate unit and the vicinal carbonyl group. **LUMO+2**: σ^* orbital on the dithiolate ring. Isosurface value = 0.04 a.u.

Frontier MOs of conformer (*M*)-**3-*eq*** are similar to those of conformation (*M*)-**3-*ax***.

We further investigate the structural and chiroptical properties of species **2**. According to the DFT calculations, eight relevant conformations range within an energy gap of 0.5 kcal mol⁻¹ and are thus likely present in solution at room temperature (Figure 20). The interconversion of these conformers involve the flipping of (i) the ethylene bridge of the TTF unit (as in the *M*-**2_I** and *M*-**2_II**; *M*-**2_III** and *M*-**2_IV**; *M*-**2_III** and *M*-**2_IV**; *M*-**2_VII** and *M*-**2_VII** pair), (ii) the TTF unit (as in the *M*-**2_I** and *M*-**2_VIII**; *M*-**2_II** and *M*-**2_VII**; *M*-**2_III** and *M*-**2_VI**; *M*-**2_IV** and *M*-**2_V** pairs) and (iii) of the terminal ring contained in the spiro fragment (as in the *M*-**2_II** and *M*-**2_III**; *M*-**2_VI** and *M*-**2_VII** pairs).

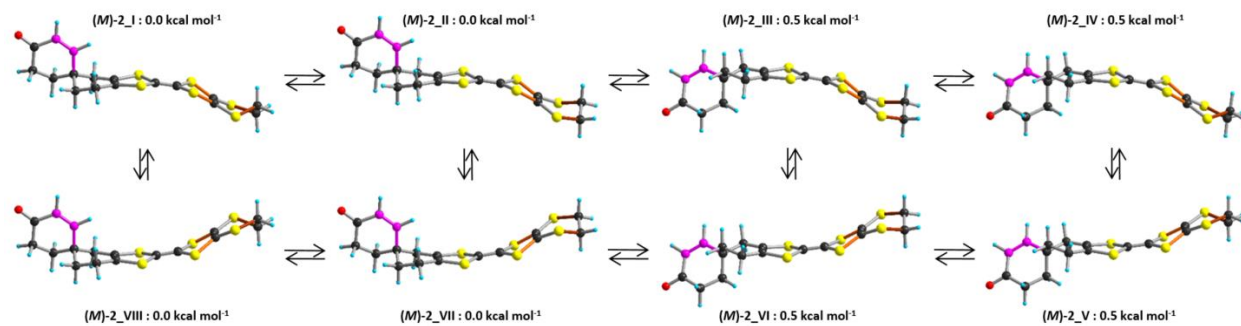


Figure 20. Equilibrium geometries of the eight conformers determined for *M*-**2** enantiomer, together with their computed relative energies.

The theoretical CD and adsorption spectra calculated for the eight relevant conformers of enantiomer (*M*)-**2** are depicted in Figure 21. Similar to the case of (*M*)-**3-*ax*** and (*M*)-**3-*eq*** conformations, it is highlighted that the CD waves computed for different conformers of (*M*)-**2** can exhibit opposite sign. This leads to the cancellation of CD signals, which results into a low intensity experimental CD spectrum. More precisely, flipping the ethylene bridge of the TTF fragment changes the sign of the bands located in the range of low energies (at *ca.* 375 and 325 nm, respectively) as well as of the CD wave computed at *ca.* 255 nm. Upon flipping the lateral ring of the spiro fragment, the CD signals at *ca.* 295 and 225 nm change their sign, while the flipping of the TTF moiety has basically no impact on the CD activity.

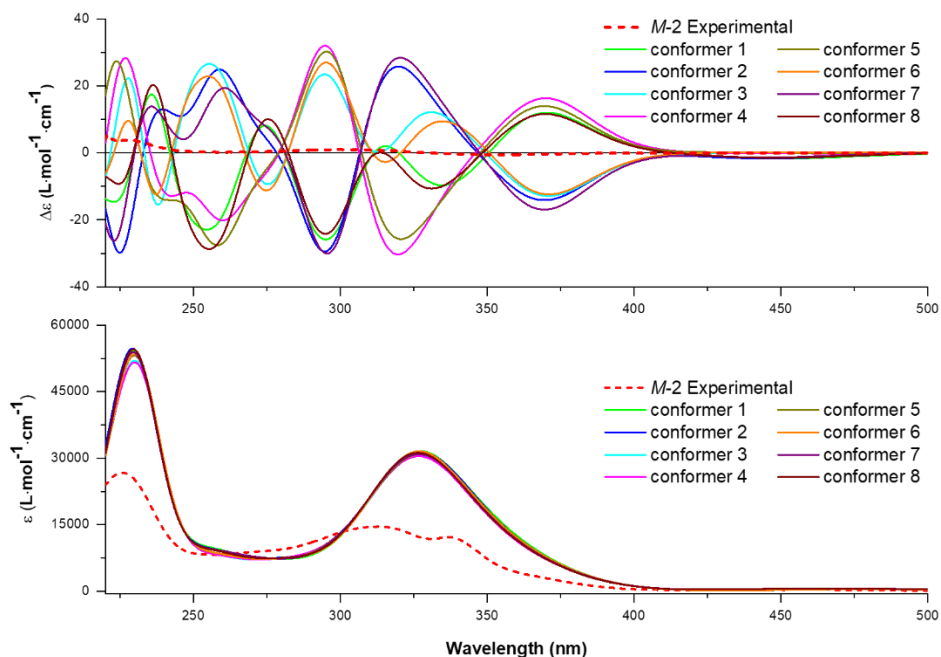


Figure 21. Theoretical CD (*above*) and absorption (*bottom*) spectra computed for the eight conformers of **M-2**. The experimental spectra of **M-2** are illustrated for comparisons.

Charge transfer complexes

Chemical oxidation of spiro-TTF **2**, both racemic and enantiopure, with TCNQF₄ provided charge transfer complexes. **Rac-2** gave a mixture of two charge transfer complexes of 1:1 stoichiometry between the donor and the acceptor. The two complexes crystallize in the centrosymmetric triclinic *P*-1 space group from dichloromethane solutions and have been separated by shape difference (narrow and wide plates Figure 22, Table S16). In one case the asymmetric units is formed of one donor and one acceptor with orthogonal disposition (**[rac-2]TCNQF₄ - I**), whereas in the other case, two donors and two acceptor molecules showed an *edge-to-edge* arrangement (**[rac-2]TCNQF₄ - II**)

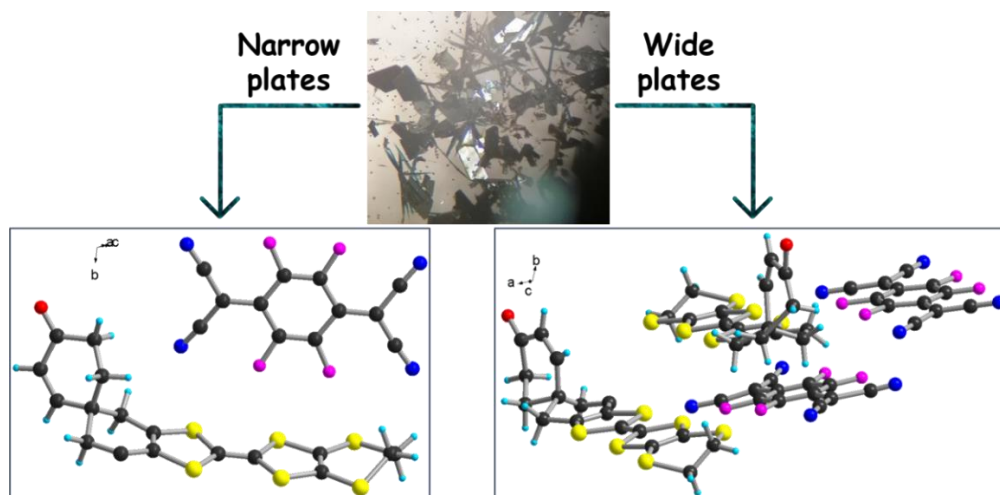


Figure 22. Crystals of the charge transfer complexes (top) and the asymmetric unit cell of the obtained phases with 1:1 stoichiometry (left, $[rac-2]TCNQF_4 - I$ and right, $[rac-2]TCNQF_4 - II$). For the $[rac-2]TCNQF_4 - II$ the disordered atoms are omitted for clarity.

In the structure of $[rac-2]TCNQF_4 - I$ complex, formed of alternating dimers of donor and acceptor disposed orthogonally, shows (spiro)CH₂⋯N and (dithiin)CH₂⋯F hydrogen bonding interactions in the packing (Figure S42). The donor molecules interact by S⋯S short contacts intradimer of 3.5 – 3.6 Å and interdimer of 3.95 Å (Figure S43).

The structure of the second complex $[rac-2]TCNQF_4 - II$ is formed of alternating slipped columns of donor and acceptor molecules (Figure 23, left). The intermolecular S⋯S interactions between the spiro-TTF molecules along the columns are comprised in the range of 3.7 – 3.9 Å (Figure 23, right).

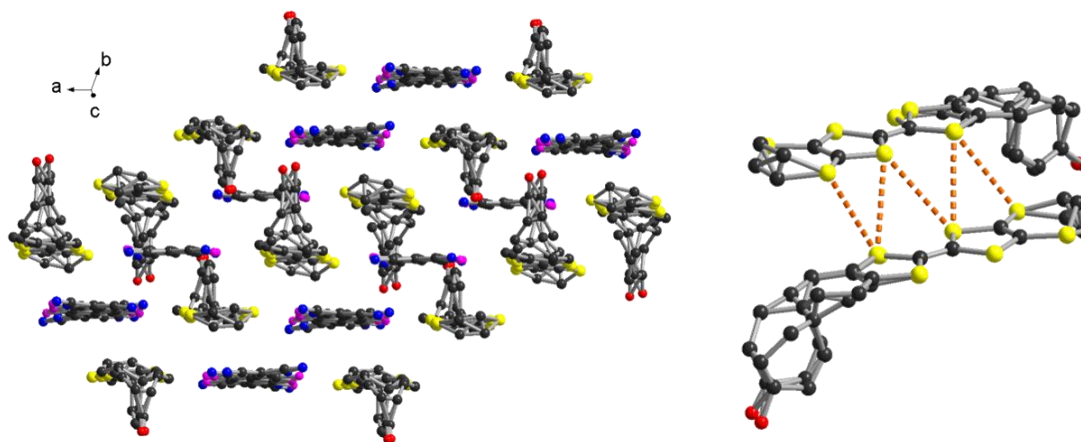


Figure 23. Packing structure (left) and S...S intermolecular interactions between the donor molecules (right) of the second charge transfer complex [*rac*-2]TCNQF₄ – II. Hydrogen atoms were omitted for clarity.

Similarly to racemic donor, the enantiopures of **2** form charge transfer complexes with TCNQF₄ by evaporation from chloroform solutions. They crystallize in the triclinic non-centrosymmetric *P1* space group with either two or four independent TTF and TCNQF₄ units in a 1:1 ratio, thus affording [*P*-2][CHCl₃]TCNQF₄ and [*M*-2]TCNQF₄ (Table S17, Figure S44). This donor forms as well a 1:1 charge transfer complex with TCNQF₂. The [*P*-2]TCNQF₂ crystallized in the triclinic non-centrosymmetric *P1* space group with two donor molecules and two acceptor molecules displayed in a criss-cross manner (Table S17, Figure S45). The packing of the complex shows molecules organized in alternated slipped columns of donors and acceptors. The columns of donors are formed by slipped dimers due to S...S contacts of 3.65 Å (orange dotted lines) and 4.05 Å (pink dotted lines) interacting laterally through S...S contacts of 3.88 Å (Figure 24).

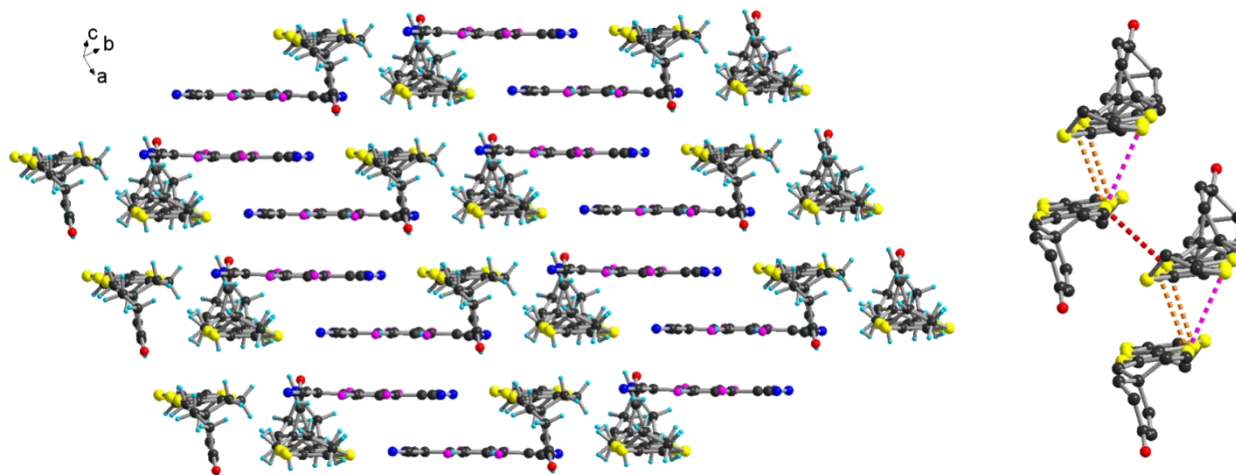


Figure 24. Packing structure of [*P*-2]TCNQF₂ (left) and short interactions between the donor molecules (right).

The C=C and C–S internal bond distances of the TTF units of the charge transfer complexes suggest a +1-oxidation state of the donors, with a complete charge transfer between the species (Table S18). The +1 oxidation state is in agreement with the conductivity measurement (Figure S46) done on the two enantiopure complexes obtained with **TCNQF₄**. Resistivity measurements on [**M-2**]**TCNQF₄** and [**P-2**]**TCNQF₄** single crystals showed semiconducting behaviour of both forms. The room temperature conductivity of both enantiomers is comparable, with values of around 10^{-6} S cm⁻¹.

Conclusions

In this study, the synthesis and characterisation of spiro-based intermediates, TTFs and charge transfer complexes have been done both experimentally and theoretically. The use of racemic spiro[5.5]undeca-1,8-dien-3-one afforded chiral derivatives bearing spiro alone and spiro plus stereogenic centres units. The mixtures of the obtained stereoisomers have been successfully separated by chiral chromatography affording two (*M* / *P*) and four (*R,S,P* / *S,R,M* and *S,R,P* / *R,S,M*) stereoisomers for both the intermediate dithiol(thi)ones (**5** and **3**) and the TTFs (**1** and **2**). Candidates of racemic and enantiopure forms of each class of derivatives have been successfully characterized by single crystal diffraction allowing the assignment of the absolute configuration of the stereoisomers which was further supported by calculations. The experimental and calculated CD characterisations revealed a predominant contribution of the (*R,S* / *S,R*) configuration in the low energy region and of the spiro (*M* / *P*) in the high energy region for the four stereoisomers of both **5** and **1** derivatives. The two classes of molecules show differences in the optical activity between the spiro alone and spiro plus stereogenic centers. The in-depth DFT and TD-DFT study revealed four notable conformers for each enantiomer of the derivatives bearing three chiral centres (**5**) and two conformations (with axial and equatorial disposition of the C=C of the spiro unit) for the spiro alone based chirality (**3**). According to calculations, the low optical activity of the spiro dithiolones **3** is due to the contribution of both *ax* and *eq* conformers which have opposite Cotton effect. The same results were obtained with the *M* enantiomer of TTF **2** for which eight notable conformers have been observed and optimized. Spiro TTF **2** has been used as donor for charge transfer complexes with TCNQ type acceptors. Racemic and enantiopures provided 1:1 CT complexes with **TCNQF₄** and **TCNQF₂** showing semiconducting behaviour. These results open

the way towards the use of the spiro-TTF precursors and derived CT complexes and radical cation salts as materials for the observation of the CISS and eMChA effects.

Experimental section

The synthesis protocol of intermediate *rac-4* together with the general methods and materials, crystallography and computational details are given in the supplementary material.

2-thioxo-5,7,8,8a-tetrahydro-4aH-spiro[benzo[b][1,3]dithiolo[4,5-e][1,4]dithiine-6,1'-cyclohex[2]en]-4'-one (*rac-5A* and *rac-5B*): Spiro derivative 6 (1.5 g, 9.2 mmol) was solubilized in 50 mL toluene. 0.9 g (4.6 mmol) of 1,3-dithiolane-2,4,5-trithione was added and the mixture was refluxed overnight. Another portion of 0.9 g (9.2 mmol in total) of 1,3-dithiolane-2,4,5-trithione was added and the mixture further refluxed for 18 hours. After the evaporation of the solvent under vacuum, dichloromethane was added and the mixture was filtered. The filtrate was chromatographed (silicagel, PE/EtOEt = 1/1 and EtOEt) and 0.7 g (21%) of a dark yellow fluffy solid were obtained, consisting in two sets of enantiomers. The mixture of four stereoisomers was further separated through semi-preparative chromatography (Chiralpak IH, EtOH/DCM = 50/50), with an ee > 99.5% each. **MS (MALDI⁺):** m/z calcd. for C₁₄H₁₄OS₅: 357.9, found 357.9; **Elemental analysis:** Calcd for C₁₄H₁₄OS₅: C, 46.9; H, 3.94; S, 44.71. Found: C, 46.70; H, 3.84; S, 44.46.

***rac-5A*:** yellow solid, R_f = 0.46 (silicagel, EtOEt), m.p.= 175-176 °C; **¹H NMR (300 MHz, CDCl₃)** δ ppm: 7.05 (d, J = 10.4 Hz, 1H), 6.01 (d, J = 10.3 Hz, 1H), 4.05 (d, J = 3.2 Hz, 1H), 3.65 (dt, J = 12.0, 3.6 Hz, 1H), 2.58 – 2.47 (m, 2H), 2.36 – 1.76 (overlapped signals, 8H); **¹³C NMR (76 MHz, CDCl₃):** 208.31, 198.38, 152.46, 129.60, 124.17, 120.48, 45.85, 40.82, 40.14, 37.41, 37.33, 33.77, 30.67, 27.12.

***rac-5B*:** dark yellow solid, R_f = 0.54 (silicagel, EtOEt), m.p.= 183-184 °C; **¹H NMR (300 MHz, CDCl₃)** δ ppm: 6.61 (d, J = 10.1 Hz, 1H), 5.93 (d, J = 10.2 Hz, 1H), 4.00 (d, J = 3.1 Hz, 1H), 3.62 (ddd, J = 12.0, 4.5, 2.4 Hz, 1H), 2.44 (t, J = 6.8 Hz, 2H), 2.28 – 1.79 (overlapped signals, 8H); **¹³C NMR (76 MHz, CDCl₃):** 208.24, 198.59, 157.10, 128.46, 124.14, 120.33, 45.35, 40.14, 38.34, 37.69, 33.51, 29.86, 28.58, 26.91.

2-(5,6-dihydro-[1,3]dithiolo[4,5-b][1,4]dithiin-2-ylidene)-5,7,8,8a-tetrahydro-4aH-spiro[benzo[b][1,3]dithiolo[4,5-e][1,4]dithiine-6,1'-cyclohex[2]en]-4'-one (*rac*-1): A mixture of 300 mg (0.84 mmol) of the four stereoisomers of spiro derivative 5 was solubilized in 10 ml trimethyl phosphite. 348 mg (1.67 mmol) of ethylenedithiolone was added and the solution was refluxed until complete consumption of the spiro derivative (10 minutes – TLC monitoring). After the solution was cooled down at room temperature, toluene was added, the mixture was filtered and the filtrate evaporated. Product was purified through column chromatography (silicagel, EtOEt) as a pink-orange solid (182 mg, 42%). The mixture of four isomers was separated through semi-preparative chromatography (Chiralpak IH and Chiralpak IC, EtOH/DCM = 50/50), with an ee > 99.5% each. **HRMS: (MALDI⁺):** m/z calcd. for C₁₉H₁₈OS₈: 517.9117, found [M]⁺: 517.9122 (error 0.88 ppm).

***rac*-1A:** orange solid, R_f = 0.50 (silicagel, EtOEt), m.p.= 214-215 °C; **¹H NMR (300 MHz, CDCl₃)** δ ppm: 7.04 (d, J = 10.4 Hz, 1H), 5.99 (d, J = 10.3 Hz, 1H), 3.95 (d, J = 3.4 Hz, 1H), 3.56 (dt, J = 11.9, 3.6 Hz, 1H), 2.56 – 2.44 (m, 2H), 2.30 – 1.75 (overlapped signals, 8H); **¹³C NMR (76 MHz, CDCl₃):** 198.71, 153.15, 129.38, 115.88, 113.94, 46.35, 41.23, 39.77, 37.35, 37.16, 33.83, 30.79, 30.31, 27.01.

***rac*-1B:** pink solid, R_f = 0.44 (silicagel, EtOEt), m.p.= 211-212 °C; **¹H NMR (300 MHz, CDCl₃)** δ ppm: 6.61 (d, J = 10.2 Hz, 1H), 5.91 (d, J = 10.2 Hz, 1H), 3.90 (d, J = 3.4 Hz, 1H), 3.53 (dt, J = 11.9, 3.6 Hz, 1H), 2.52 – 2.36 (m, 2H), 2.26 – 1.70 (overlapped signals, 8H); **¹³C NMR (76 MHz, CDCl₃):** 198.92, 157.71, 128.21, 115.90, 113.91, 111.36, 45.87, 40.53, 37.88, 37.52, 33.60, 30.30, 29.89, 28.74, 26.81.

6,7-dihydro-4H-spiro[benzo[d][1,3]dithiole-5,1'-cyclohex[2]ene]-2,4'-dione (*rac*-3): A solution of 0.9 g (5.13 mmol) of freshly prepared PIPX (potassium isopropyl xanthate) in acetone was added dropwise over a solution of 1.2 g (4.66 mmol) of mixture of *rac*-4 in acetone. The resulting solution was stirred at room temperature until no more starting material was observed (TLC monitoring – approx. 4 hours). After the solvent evaporation water was added and the product was extracted with diethyl ether (1.4 g of a pale-yellow oil, 96%).

The spiro isopropyl xanthate derivative was further suspended in conc. H₂SO₄ on an ice bath and stirred at 0°C for 15 min and for 2 hours at room temperature. The mixture was then poured in

crushed ice, extracted with diethyl ether and the organic phase was washed with water and dried over anhydrous MgSO_4 . After the evaporation of the solvent, the residue was chromatographed (silicagel, PE/EtOAc = 3/2) and the spiro derivative *rac*-3 was obtained as a white solid (0.85 g, 75%, R_f = 0.17, silicagel, PE/EtOAc = 3/1) with m.p. = 110-111 °C; $^1\text{H NMR}$ (300 MHz, CDCl_3) δ ppm: 6.80 (d, J = 10.2 Hz, 1H), 6.01 (dd, J = 10.2, 1.0 Hz, 1H), 2.62 – 2.44 (overlapped signals, 6H), 2.16 – 2.02 (m, 2H), 2.01 – 1.78 (m, 2H); $^{13}\text{C NMR}$ (76 MHz, CDCl_3): 198.48, 191.77, 154.35, 129.32, 124.97, 123.25, 35.42, 35.37, 33.63, 32.59, 32.51, 22.99; **HRMS: (EI⁺)**: m/z calcd. for $\text{C}_{12}\text{H}_{12}\text{O}_2\text{S}_2$: 252.0279, found $[\text{M}]^+$: 252.0823 (error 1.7 ppm); **Elemental analysis**: Calcd for $\text{C}_{12}\text{H}_{12}\text{O}_2\text{S}_2$: C, 57.12; H, 4.79; S, 25.41. Found: C, 57.34; H, 4.82; S, 25.23.

2-(5,6-dihydro-[1,3]dithiolo[4,5-b][1,4]dithiin-2-ylidene)-6,7-dihydro-4H-

spiro[benzo[d][1,3]dithiole-5,1'-cyclohex[2]en]-4'-one (*rac*-2): A solution of 400 mg (1.6 mmol) of spiro dithiolene *rac*-4 and 710 mg (3.2 mmol) of ethylenedithiothione in 10 mL $\text{P}(\text{OMe})_3$ was stirred at 110 °C for 5 hours. Toluene was added, the formed precipitate was filtrated and the filtrate was separated through column chromatography (silicagel, EtOEt/PE = 2/1 and CH_2Cl_2). The product was obtained as a pink solid (20 mg, 3%) with a R_f = 0.31 (silicagel, CH_2Cl_2) and m.p. = 181-182 °C. The enantiomers were separated through semi-preparative chromatography (Chiralpak IH EtOH/DCM = 50/50), with an ee > 99.5% each. $^1\text{H NMR}$ (300 MHz, CDCl_3) δ ppm: 6.75 (d, J = 10.2 Hz, 1H), 5.98 (d, J = 10.2 Hz, 1H), 2.54 – 2.44 (m, 2H), 2.42 – 2.27 (overlapped signals, 4H), 2.08 – 1.84 (overlapped signals, 3H), 1.76 (dd, J = 13.3, 6.8 Hz, 1H); $^{13}\text{C NMR}$ (76 MHz, CDCl_3): 198.77, 155.02, 129.24, 125.36, 123.79, 116.24, 114.21, 105.42, 35.65, 35.45, 33.87, 32.60, 30.38; **HRMS: (MALDI⁺)**: m/z calcd. for $\text{C}_{17}\text{H}_{16}\text{OS}_6$: 427.9519, found $[\text{M}]^+$: 427.9523 (error 0.64 ppm).

Acknowledgements

This work was supported in France by Campus France and the University of Angers through the Eiffel scholarship and the RFI-LUMOMAT for the 3 months funding for Alexandra Bogdan, and by GDR Chirafun. Magali Allain (MOLTECH-Anjou) is gratefully acknowledged for help with the refinement of the crystal structures and Ingrid Freuze (SFR MATRIX, University of Angers) is acknowledged for MS characterization. The authors would also like to thank for the computational resources provided by the high-performance computational facility of the Babeş-Bolyai University (MADECIP, POSCCE, COD SMIS 48801/1862).

Conflict of Interest

There are no conflicts to declare.

Data Availability Statement

The data that support the findings of this study are available in the supplementary material of this article.

Keywords

chirality

tetrathiafulvalene

spiro compounds

TD-DFT calculations

circular dichroism

References

-
- [1] F. Pop, N. Zigon, N. Avarvari, *Chem. Rev.* **2019**, *119*, 8435–8478.
 - [2] G. L. J. A. Rikken, J. Fölling, P. Wyder, *Phys. Rev. Lett.* **2001**, *87*, 236602.
 - [3] G. L. J. A. Rikken, N. Avarvari, *Nat. Commun.* **2022**, *13*, 3564.
 - [4] R. Naaman, Y. Paltiel, D. H. Waldeck, *Nat. Rev. Chem.* **2019**, *3*, 250–260.
 - [5] P. Chandra Mondal, N. Kantor-Uriel, S. P. Mathew, F. Tassinari, C. Fontanesi, R. Naaman, *Adv. Mater.* **2015**, *27*, 1924–1927.
 - [6] R. Naaman, Y. Paltiel, D. H. Waldeck, *J. Phys. Chem. Lett.* **2020**, *11*, 3660–3666.
 - [7] G. L. J. A. Rikken, N. Avarvari, *J. Phys. Chem. Lett.* **2023**, *14*, 9727–9731.
 - [8] E. M. Carnicom, W. Xie, T. Klimczuk, J. Lin, K. Górnicka, Z. Sobczak, N. P. Ong, R. J. Cava, *Sci. Adv.* **2018**, *4*, eaar7969.
 - [9] N. Mroweh, C. Mézière, F. Pop, P. Auban-Senzier, P. Alemany, E. Canadell, N. Avarvari, *Adv. Mater.* **2020**, *32*, 2002811.
 - [10] F. Qin, W. Shi, T. Ideue, M. Yoshida, A. Zak, R. Tenne, T. Kikitsu, D. Inoue, D. Hashizume, Y. Iwasa, *Nat. Commun.* **2017**, *8*, 14465.
 - [11] R. Nakajima, D. Hirobe, G. Kawaguchi, Y. Nabei, T. Sato, T. Narushima, H. Okamoto, H. M. Yamamoto, *Nature* **2023**, *613*, 479–484.

-
- [12] N. Avarvari, J. D. Wallis, *J. Mater. Chem.* **2009**, *19*, 4061–4076.
- [13] F. Pop, P. Auban-Senzier, A. Frąckowiak, K. Ptaszyński, I. Olejniczak, J. D. Wallis, E. Canadell, N. Avarvari, *J. Am. Chem. Soc.* **2013**, *135*, 17176–17186.
- [14] N. Mroweh, P. Auban-Senzier, N. Vanthuyne, E. Canadell, N. Avarvari, *J. Mater. Chem. C* **2019**, *7*, 12664–12673.
- [15] J. D. Dunitz, A. Karrer, J. D. Wallis, *Helv. Chim. Acta* **1986**, *69*, 69–70.
- [16] S. Matsumiya, A. Izuoka, T. Sugawara, T. Taruishi, Y. Kawada, *Bull. Chem. Soc. Jpn.* **1993**, *66*, 513–522.
- [17] F. Pop, P. Auban-Senzier, E. Canadell, N. Avarvari, *Chem. Commun.* **2016**, *52*, 12438–12441.
- [18] N. Mroweh, T. Cauchy, N. Vanthuyne, N. Avarvari, *CrystEngComm* **2022**, *24*, 6187–6197.
- [19] A. Karrer, J. D. Wallis, J. D. Dunitz, B. Hilti, C. W. Mayer, M. Bürkle, J. Pfeiffer, *Helv. Chim. Acta* **1987**, *70*, 942–953.
- [20] S. Yang, F. Pop, C. Melan, A. C. Brooks, L. Martin, P. Horton, P. Auban-Senzier, G. L. J. A. Rikken, N. Avarvari, J. D. Wallis, *CrystEngComm* **2014**, *16*, 3906–3916.
- [21] J. R. Galán-Mascarós, E. Coronado, P. A. Goddard, J. Singleton, A. I. Coldea, J. D. Wallis, S. J. Coles, A. Alberola, *J. Am. Chem. Soc.* **2010**, *132*, 9271–9273.
- [22] L. Martin, H. Akutsu, P. N. Horton, M. B. Hursthouse, *CrystEngComm* **2015**, *17*, 2783–2790.
- [23] T. J. Blundell, M. Brannan, H. Nishimoto, T. Kadoya, J. Yamada, H. Akutsu, Y. Nakazawa, L. Martin, *Chem. Commun.* **2021**, *57*, 5406–5409.
- [24] T. J. Blundell, J. R. Lopez, K. Sneade, J. D. Wallis, H. Akutsu, Y. Nakazawa, S. J. Coles, C. Wilson, L. Martin, *Dalton Trans.* **2022**, *51*, 4843–4852.
- [25] F. Pop, P. Auban-Senzier, E. Canadell, G. L. J. A. Rikken, N. Avarvari, *Nat. Commun.* **2014**, *5*, 3757.
- [26] A. Stefani, A. Bogdan, F. Pop, F. Tassinari, L. Pasquali, C. Fontanesi, N. Avarvari, *J. Chem. Phys.* **2023**, *159*, 204706.
- [27] C. Kulkarni, A. K. Mondal, T. K. Das, G. Grinbom, F. Tassinari, M. F. J. Mabeoone, E. W. Meijer, R. Naaman, *Adv. Mater.* **2020**, *32*, 1904965.
- [28] D. Amsallem, A. Kumar, R. Naaman, O. Gidron, *Chirality* **2023**, *35*, 562–568.

-
- [29] T. Biet, A. Fihey, T. Cauchy, N. Vanthuyne, C. Roussel, J. Crassous, N. Avarvari, *Chem. Eur. J.* **2013**, *19*, 13160–13167.
- [30] M. Hasegawa, Y. Sone, S. Ywata, H. Matsuzawa, Y. Mazaki, *Org. Lett.* **2011**, *13*, 4688–4691.
- [31] Y. Zhou, D. Zhang, L. Zhu, Z. Shuai, D. Zhu, *J. Org. Chem.* **2006**, *71*, 2123–2130.
- [32] A. Saad, F. Barrière, E. Levillain, N. Vanthuyne, O. Jeannin, M. Fourmigué, *Chem. Eur. J.* **2010**, *16*, 8020–8028.
- [33] M. Nógrádi, L. Poppe, J. Nagy, G. Hornyánszky, Z. Boros, *Stereochemistry and Stereoselective Synthesis: An Introduction*, Wiley-VCH Verlag GmbH & Co., Weinheim, **2016**.
- [34] E. Nishikawa, H. Tatemitsu, Y. Sakata, S. Misumi *Chem. Lett.* **1986**, 2131–2134.
- [35] P. Sandín, A. Martínez-Grau, L. Sánchez, C. Seoane, R. Pou-Amérigo, E. Ortí, N. Martín, *Org. Lett.* **2005**, *7*, 295–298.
- [36] M. Hasegawa, D. Kurebayashi, H. Matsuzawa, Y. Mazaki, *Chem. Lett.* **2018**, *47*, 989–992.
- [37] J.-P. Griffiths, H. Nie, R. J. Brown, P. Day, J. D. Wallis, *Org. Biomol. Chem.* **2005**, *3*, 2155–2166.
- [38] N. Xu, R. Wang, F. S. Du, Z. C. Li, *J. Polym. Sci. Part A: Polym. Chem.* **2009**, *47*, 3583–3594.
- [39] A. Abhervé, N. Mroweh, T. Cauchy, F. Pop, H.-B. Cui, R. Kato, N. Vanthuyne, P. Alemany, E. Canadell, N. Avarvari, *J. Mater. Chem. C* **2021**, *9*, 4119–4140.

Entry for the Table of Contents

Spiro-TTFs have been characterized experimentally and theoretically, and the formation of charge transfer complexes with TCNQF₂ and TCNQF₄ has been reported. The chiroptical investigation of the neutral systems revealed significant differences in chiroptical activity depending on the nature of chiral centres and between diastereomers.

